


Research Article

Vibration Reduction Design and Test of UAV Load Radar

Jia Fu,^{1,2} Chaohui Fan,^{1,2,3} Changshuai Yu,^{1,2} Guangming Liu,^{1,2} and Haitao Luo ^{1,2}

¹State Key Laboratory of Robotics, Shenyang Institute of Automation, Chinese Academy of Sciences (CAS), Shenyang 110016, China

²Institutes for Robotics and Intelligent Manufacturing, Chinese Academy of Sciences, Shenyang 110169, China

³University of Chinese Academy of Sciences, Beijing 100049, China

Correspondence should be addressed to Haitao Luo; luohaitao@sia.cn

Received 21 June 2022; Revised 23 October 2022; Accepted 16 November 2022; Published 2 December 2022

Academic Editor: Zhiguang Song

Copyright © 2022 Jia Fu et al. This is an open access article distributed under the Creative Commons Attribution License, which permits unrestricted use, distribution, and reproduction in any medium, provided the original work is properly cited.

It is challenging to design complex structures and calculate their dimensions only on the basis of theory. This issue was resolved efficiently by the FEM. Using the applicable test, the mechanical properties of the materials used in the damper are estimated, effectively guiding the design of the device and boosting its vibration-reducing performance. A large-load unmanned aerial vehicle (UAV) airborne radar is the subject of this research article. According to particular use case, vibration dampers for the radar-mounting platform are designed using passive vibration isolation technology to reduce aircraft vibration transmission to the radar. A conference paper has already presented prior research on the same topic. Earlier research confirmed the vibration-isolating efficacy of the T-type rubber isolator, which can greatly improve the operational conditions of the airborne radar. In contrast, earlier studies relied more on experimental validation and did not use numerical simulations. This research's primary objective is the development of a T-type rubber isolator, whose vibration reduction performance is proven using FEM and experiments. Utilizing a suitable simulation analysis method to investigate the vibration reduction of an unmanned aerial vehicle's (UAV) airborne component is a crucial technical task. By comparing multiple material models, a more precise model for characterizing rubber was developed.

1. Introduction

Due to advancements in communication capability and control algorithm development, the UAV business is increasing rapidly. UAVs are flexible because they may be remotely commanded and carry a range of mission equipment. On the one hand, the primary military applications of unmanned aerial vehicles are the detection of hostile activity, the delivery of alarms, and the relay of communications. On the other hand, the principal applications of UAVs in the civilian sector are plant cultivation, disaster assessment, forest fire control, and artificial precipitation [1–3]. Typically, UAVs are equipped with optical instruments, radar, inertial measurement units (IMUs), and other sensors for data collecting and flight control [4–7]. The precision of the data collected by these sensors affects the UAV's ability to control its flight and complete its mission.

The high-frequency vibrations generated by the operation of the UAV engine are a significant external component that

affects the accuracy of the data. In the absence of sufficient damping in the system, high-frequency vibrations might cause sensor drift and reduce the signal's precision [8]. Combining the aforementioned factors, vibration-dampening techniques for the on-board sensing apparatus are necessary for the UAV to operate effectively in a demanding operating environment. Vibration can cause data gathered from on-board equipment to be distorted [7, 9]. There are four primary types of stabilization solutions for UAVs: optical image stabilization, digital image stabilization, inertia-based stabilization, and mechanical vibration dampening [10]. La Rosa et al. [11] outlined the fundamental framework of the control system for optical image stabilization. Voice-coil actuators [12] and piezo actuators [13] are used in a wide range of applications. The objective of digital image stabilization is to remove the effects of global motion from an image sequence, leaving only smooth camera movement [14]. It can compensate for a wide variety of vibrations, excluding only those with a large amplitude. When reliable tracking of a target is necessary, inertia-

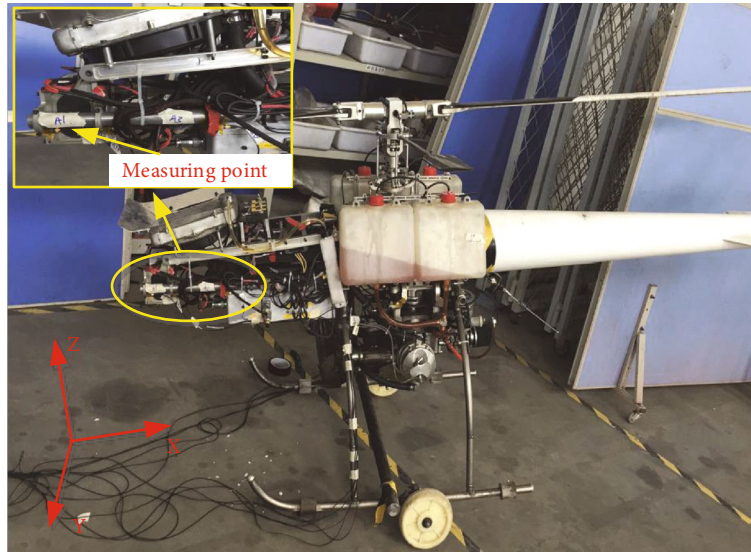


FIGURE 1: Flight vibration test.

based stabilization is most often employed. Typically, this stabilizing technology is in the form of a gimbal. Passive or active compensation methods exist [15]. Joints having a low coefficient of friction and a high internal axis of inertia can assist in passively maintaining the correct body position [16]. This stabilizing method is effective against a broad spectrum of vibrations, but not high-frequency vibrations. The three stabilizing procedures account for the effect of vibration on the measuring device to compensate for the obtained data.

The most prevalent way is isolating the collecting data device from drone vibrations. This practice is known as mechanical stabilization. It can be used alone or as a supplement to the three aforementioned techniques. According to Verma et al. [17], mechanical stabilization is the sole stabilization technique that can perform satisfactorily over the whole frequency range for all amplitudes. Passive isolation, semiactive isolation, and active isolation are the three types of mechanical stabilization procedures. Passive vibration reduction is commonly utilized, since it does not require the system to be supplied with external energy to regulate the vibration reduction device. Typically, active isolation calls for sensors, controllers, actuators, and power supply. On the one hand, active isolation systems, compared to passive isolation systems or other compensating stabilizing strategies, are more sophisticated and can result in major stability issues. On the other hand, they can greatly increase the payload's weight. A semiactive isolation method can fix a portion of the problem, but the most effective answer is to employ a passive isolation system that functions well [18].

Examples of well-known damping components include springs, dampers, rubber mounts, and viscoelastic polymers. Inspired by birds, Pete et al. [19] employed spring dampers to replicate a bird's neck, therefore isolating the payload from the drone. Patrizi et al. [7] examined the Kyosho Zeal sheet and its effectiveness in UAV vibration isolation. Using digital low-pass filters and the Kyosho Zeal sheet, they discovered a 97.1% improvement in amplitude reduction. Small size, a broad damping frequency range, and a good damping

effect at the moment of resonance are among the advantages of silicone rubber dampers, which are frequently employed in flight equipment [20–22]. Chen et al. created a rubber isolator, which was represented as a dual isolation system, to lessen the microvibration caused by the optical satellite's fly-wheel. Using theoretical reasoning, they determined an acceptable cutoff frequency for the isolator and determined the RMS attenuation of the pixel offset under the dual isolation system [23]. Chen et al. discovered that the dual isolation system was effective in isolating vibrations; however, they did not specify how accurately the dual isolation system characterized the rubber vibration isolator. Xu et al. examined rubber dampers with various substrates and discovered that the mechanical properties of silicone rubber vibration isolators are rather stable and are not significantly impacted by the frequency and amplitude of the excitation [24]. The majority of damping system designs are now based on experience and refined through trial and error. This style of design requires a great deal of time and resources. In this study, the application of numerical analysis in the early design phase and the validation of the vibration isolator are the focal points. The constitutive model of the rubber material utilized in a numerical simulation has an immediate effect on the accuracy of the simulation.

Rubber materials have complex mechanical properties. Rubber is a nearly incompressible substance. When loaded, it exhibits nonlinear elastic deformation, and when unloaded, the deformation returns to zero. As a result, its behavior is hyperelastic. Numerous hyperelastic models of rubber exist, including Arruda-Boyce [25], Neo-Hookean [26], Mooney-Rivlin [26–27], Yeoh [28], Gent [29], Blatz-Ko [30], and Ogden [31], among others. The Mooney-Rivlin model is widely employed and serves as the basis for a number of models based on strain tensor invariants. It can more correctly characterize the mechanical properties of rubber materials across a narrow range of strain (tensile strain within 100 percent and compressive strain within 30 percent). Before numerical simulations are performed on rubber materials, tensile

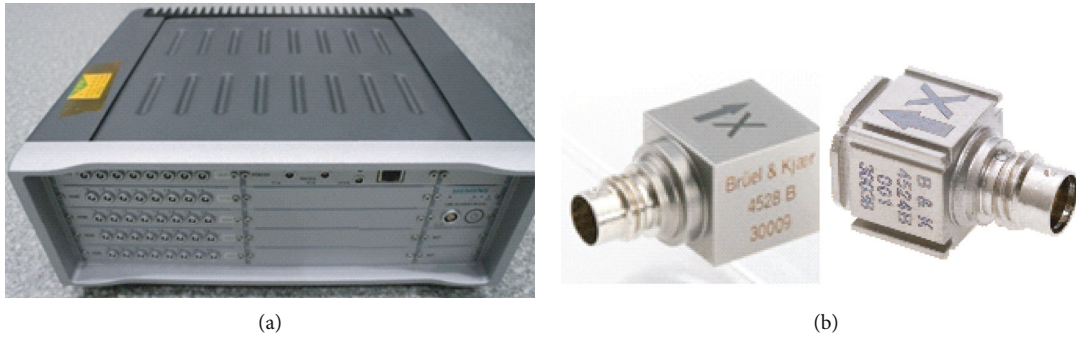


FIGURE 2: Signal acquisition equipment. (a) SCM209 data acquisition instrument. (b) Accelerometers.

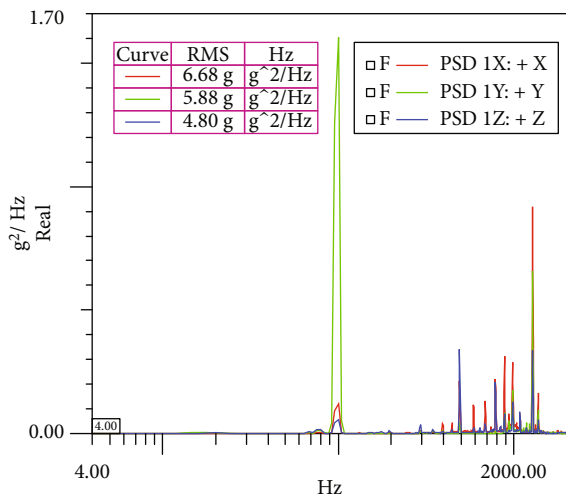


FIGURE 3: PSD response at radar installation location.

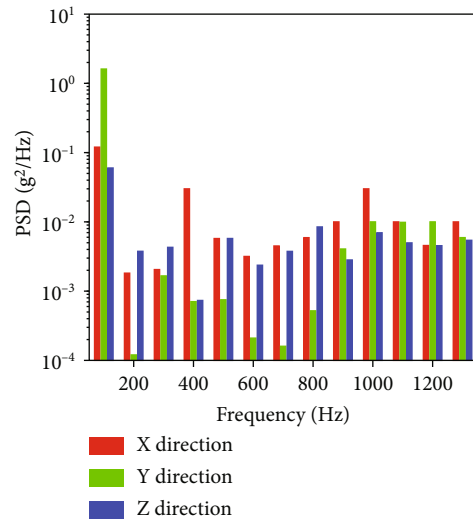


FIGURE 4: Peak frequency corresponds of power spectral density.

tests are typically performed to get the rubber’s stress-strain curves. These curves are then fitted to the hyperelastic model’s parameters [32–33]. Rubber is viscoelastic because its stress-strain relationship exhibits hysteresis and strain rate dependence under dynamic loading. The conventional integer-order viscoelastic model has been used extensively to explore viscoelastic materials [34]. Aabqus’s viscoelastic constitutive model is the generalized Maxwell model, which accurately represents the dynamic mechanical properties of rubber across a broad frequency range. Zhou et al. employed DMA to determine the viscoelastic characteristics of silicone rubber and finite element analysis to create a model of the silicone rubber vibration isolator [35]. Zhang et al. utilized DMA to determine the parameters of the generalized Maxwell viscoelastic model and control variables in order to investigate the dynamic mechanical behavior of rubber at various frequencies, temperatures, and amplitudes [36]. In the past, numerical simulations of rubber either defined just hyperelasticity and ignored viscoelasticity or defined only viscoelasticity and replaced the nonlinear stress-strain relationship of rubber with linear elasticity.

This research investigates a radar installed on a heavy payload UAV. Several typical rubber materials are summarized by analyzing the constitutive model of rubber utilized for vibration isolators. The parameters of the various constitutive models were determined by carrying out various

experiments on the rubber and fitting the test results. Then, the T-type rubber vibration isolator is analyzed by the finite element method. Finally, the T-type rubber isolator is attached to the UAV-damping platform for analysis and testing inside. The performance of the damping platform is confirmed by the UAV’s actual flight test outside.

2. Airborne Radar Vibration Test

In accordance with the description of the radar’s performance in the specification, the amplitude of impact acceleration must not exceed 30 g with a period of 11 ms, and the root-mean-square of random vibration must not exceed 3grms in the frequency range of 5 Hz to 2000 Hz. Normal operation of the radar can continue under the approved conditions.

An outside UAV flight test is conducted to examine the actual vibration acceleration response of the radar during flight. Place the acceleration sensor at the radar installation location in front of the UAV, as illustrated in Figure 1. Then, we gathered the time domain and frequency domain acceleration signals of the measurement point and examined the vibration response’s frequency component and amplitude distribution. The LMS test system was used for signal acquisition in the test. An SCM209 data acquisition front end is

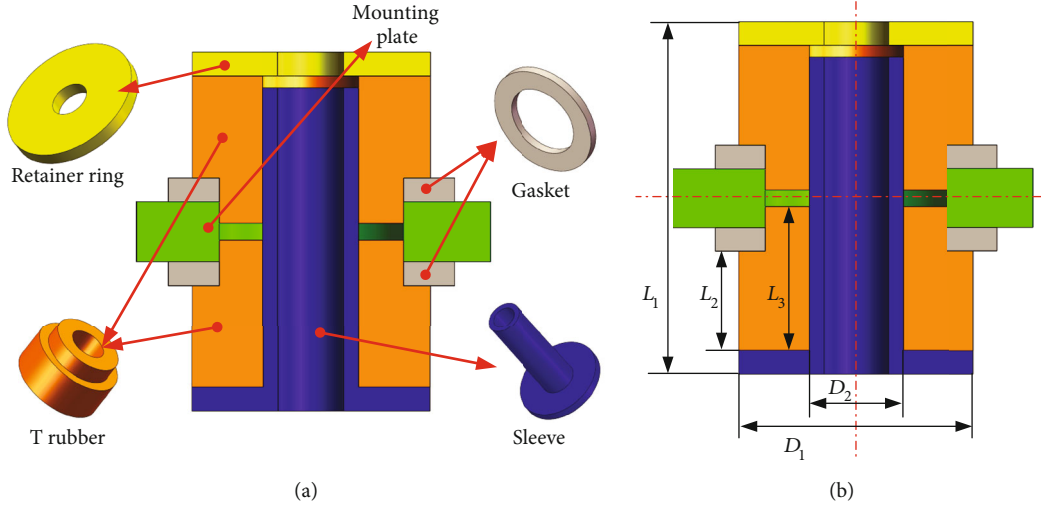


FIGURE 5: T-type rubber isolator. (a) Schematic diagram. (b) Main dimensions.

TABLE 1: Main dimensions of T-type rubber isolator.

Label	D1	D2	L1	L2	L3
Value (mm)	20	8	30	8.5	12.3

TABLE 2: Material of each component.

Component	Gasket	Sleeve	Retaining ring	Rubber
Material	Q235	Q235	Q235	ZN-37

shown in Figure 2(a). The B&K 4528-B acceleration sensor and the B&K 4524-B acceleration sensor selected for the test are shown in Figure 2(b).

Within 10 seconds of the UAV achieving flight stability, the vibration response curve is intercepted. Figure 3 depicts the power spectral density (PSD) curve of acceleration in all directions.

During operation, the maximum acceleration amplitude of the UAV is close to 40g, and the power spectral density response is 6.68g in the X direction, 5.88g in the Y direction, and 4.80g in the Z direction. Analyzing the acquired vibration response reveals that the vibration response of the radar installation position during operation exceeded its bearing capacity. If the radar is mounted directly on the UAV, it will typically fail or be damaged. To preserve it, suitable vibration isolation measures must be implemented.

In designing a vibration isolator, the frequency components of vibration response play a crucial role. As the UAV flies by rotating its propeller, its vibration manifests mostly as high-energy narrow-band random vibration or sinusoidal vibration superimposed by wide-band random vibration. Because the engine operates at full power during the flying phase, the influence of pneumatics on the UAV is minimal, and the broadband random vibration energy is low, while the sinusoidal vibration energy is considerable. As demonstrated in Figure 4, the frequency components of vibration signals in the power spectral density curve are nearly identical in all three directions and are multiples of 100 Hz.

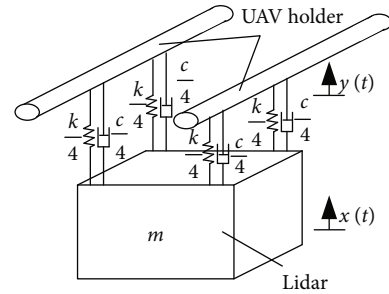


FIGURE 6: Dynamic model of airborne radar-mounting platform.

3. Design of T-Type Rubber Vibration Absorber

3.1. Structure Design. We designed a T-type rubber vibration isolator that is symmetrically mounted on the radar mounting platform. The rubber vibration absorber comprises a retaining ring, a connecting sleeve, two gaskets, and two T-type rubbers. The structural schematic is shown in Figure 5(a). Insert the connection sleeve into the mounting hole of the vibration isolation platform. The two T-shaped rubber sleeves are positioned outside of the connecting sleeve and are symmetrically oriented on both sides of the mounting hole. In addition, a gasket is positioned between the mounting plate and the T-shaped rubber on both sides. Maintain a specific distance between the retaining ring and connecting sleeve to ensure a 5% preload. In the horizontal direction, T-shaped rubber reduces vibrations more effectively. Moreover, the top and lower symmetrical structures enhance the overall damping performance and the effect of reducing unidirectional vibration. Adding a gasket between the mounting plate and the T-shaped rubber increases the bearing's rigidity and prevents the rubber from collapsing. The processing and manufacturing of the isolator is mostly determined by the size of the T-rubber and the installed size. The dimensions are shown in Figure 5(b), and the parameter values are listed in Table 1. Table 2 displays the materials used for each component.

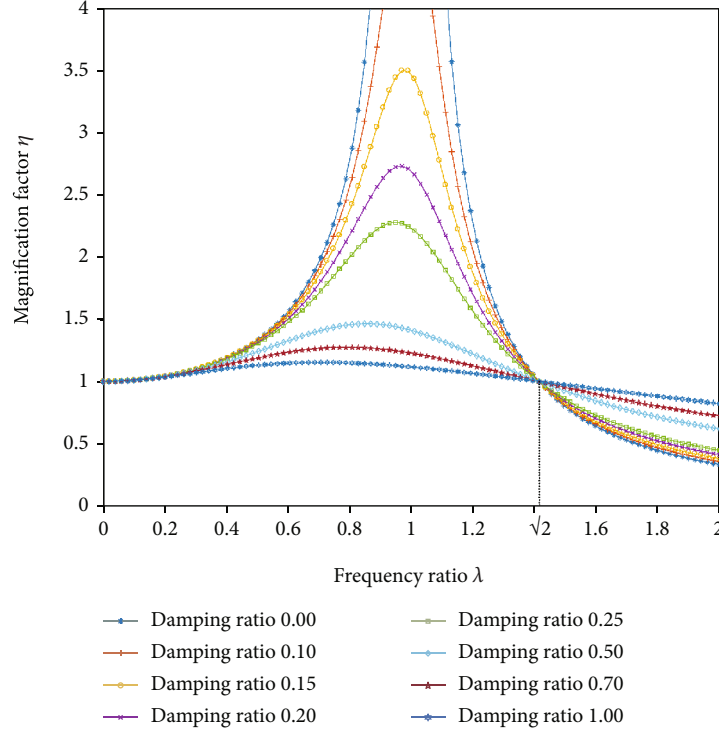


FIGURE 7: Amplitude-frequency response curve.

The next test and simulation use the rubber isolator that was made with these parameters.

3.2. Dynamic Model. In the current research, the design of the vibration reduction device focuses primarily on designing the damping structure and elastic structure between the vibration source and precision device, as well as modifying their connection qualities to weaken their dynamic coupling relationship. In our research, the UAV's engine is the cause of vibration, and the airborne radar is the device that requires vibration damping. The UAV bracket is the key structure to fixing the radar system and transmits the vibration to the radar. To simplify the vibration system, the vibration excitation in three directions might be equivalent to the vibration excitation in the horizontal and vertical directions in the spatial rectangular coordinate system.

In this paper, a vibration isolation structure is designed on the front bracket of the UAV to reduce vibration transmitted to the radar. The vibration isolation structure can be simplified into a spring-damping system. According to the dynamic model structure, the spring-damping system is divided into four groups. The dynamic model of the front-mounted radar-mounting platform is shown in Figure 6.

The vibration damping structure is simplified as a single-degree-of-freedom system, and the motion differential equation of the system is established:

$$m\ddot{x} + c(\dot{x} - \dot{y}) + k(x - y) = 0. \quad (1)$$

Assuming that the input vibration signal of the UAV bracket is simple harmonic vibration, let the input vibration

signal be $y = A \sin(\omega t)$, and the complex number method is used to solve the differential equation. Both the input displacement vibration y and the steady-state displacement response x of the radar are expressed in complex form.

$$x = ae^{i\omega t}, \quad (2)$$

$$y = Be^{i(\omega t - \theta)}. \quad (3)$$

Substitute into equation (1) and get

$$(k - m\omega^2 + ic\omega)Be^{i(\omega t - \theta)} = a(k + ic\omega)e^{i\omega t}, \quad (4)$$

$$\eta = \frac{B}{A} = \sqrt{\frac{1 + (2\xi\lambda)^2}{(1 - \lambda^2)^2 + (2\xi\lambda)^2}}, \quad (5)$$

$$\xi = \frac{c}{2\sqrt{mk}}, \quad (6)$$

where η is the displacement transfer rate, λ is the ratio of excitation frequency to the natural frequency, and ξ is the damping ratio. Take the frequency ratio λ as x -coordinate and the magnification factor η as y -coordinate to draw the amplitude-frequency response curves under different damping ratios, in which the displacement transfer rate η and frequency ratio λ are both dimensionless units, as shown in Figure 7.

It can be seen from Figure 7 that when the frequency ratio λ is greater than $\sqrt{2}$, the displacement transfer rate η for any size of the damping ratio ξ is less than 1. From the test results, we can know that the vibration response of

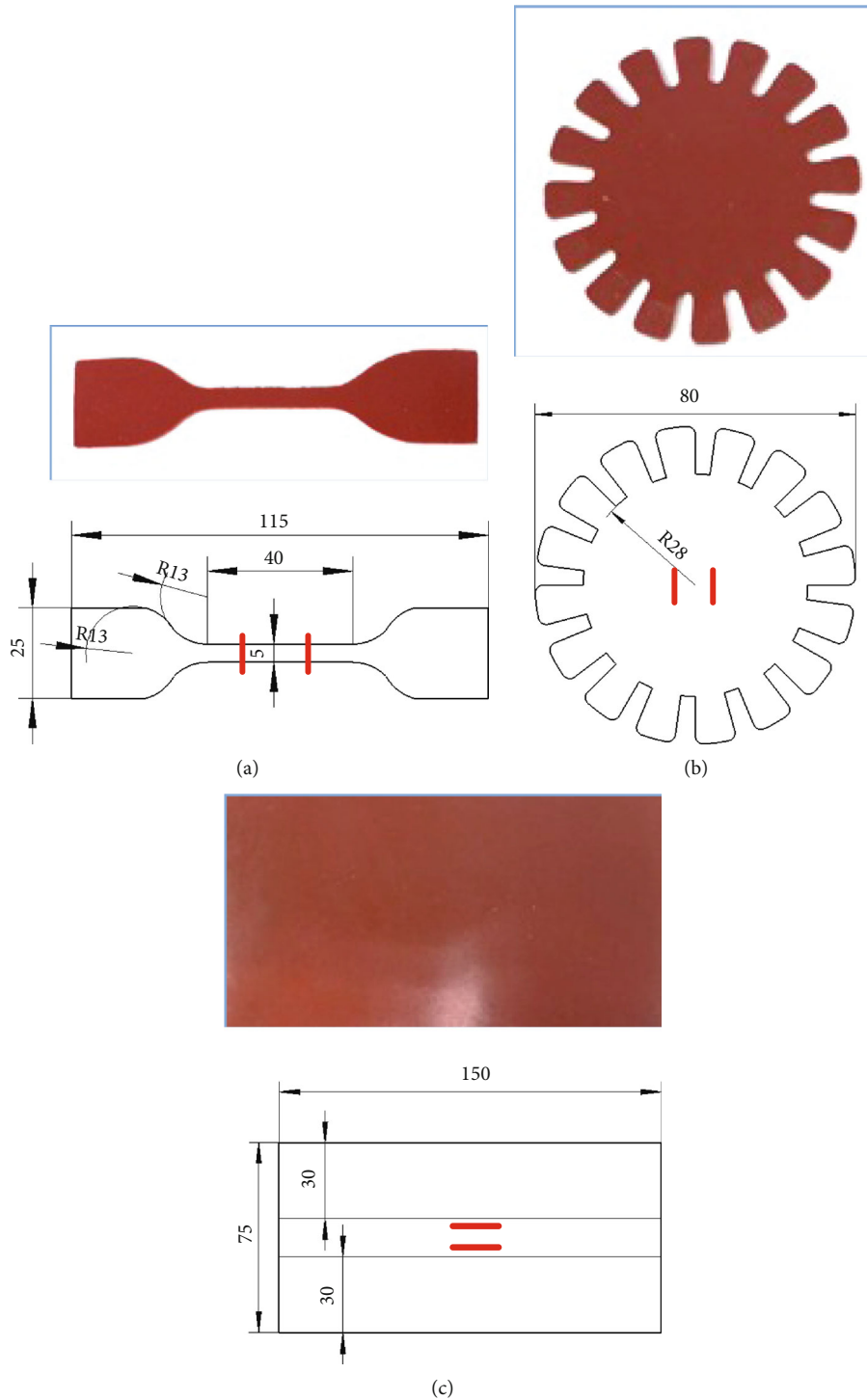


FIGURE 8: Rubber specimens and dimensions. (a) Uniaxial tensile. (b) Equal biaxial tensile. (c) Plane tensile.

UAV in actual work shows the peak response at 100 Hz and its multiple frequencies, and the PSD has a greater peak value at 100 Hz. Through the T-type rubber isolator, adjust the natural frequency of the radar structure and ensure that the transmission rate is less than one under the vibration response of the UAV. Moreover, the smaller the vibration transmission rate is, the better the vibration reduction performance of the structure will be. However, when the transmission rate is too low, the stiffness of the vibration

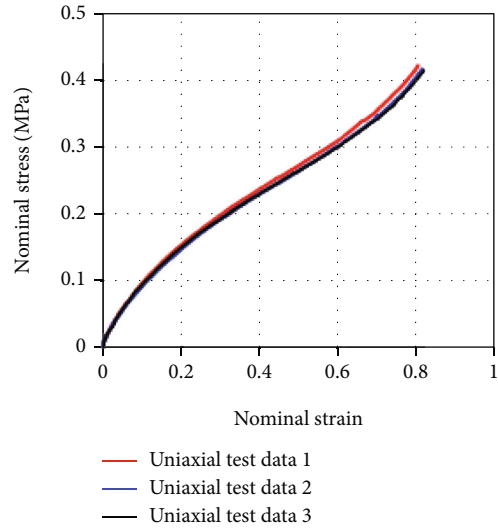
reduction structure will become smaller, making the structure unable to bear too much load and prone to strength failure, which needs to be balanced.

4. Mechanical Property Testing of Rubber Materials

In the finite element analysis of rubber structures, the choice of material model and the accuracy of material parameters



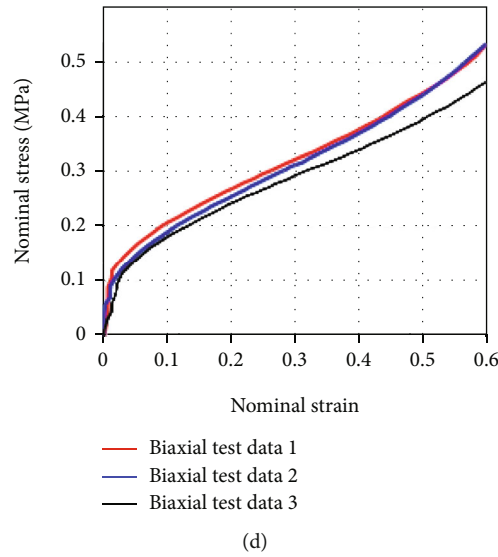
(a)



(b)



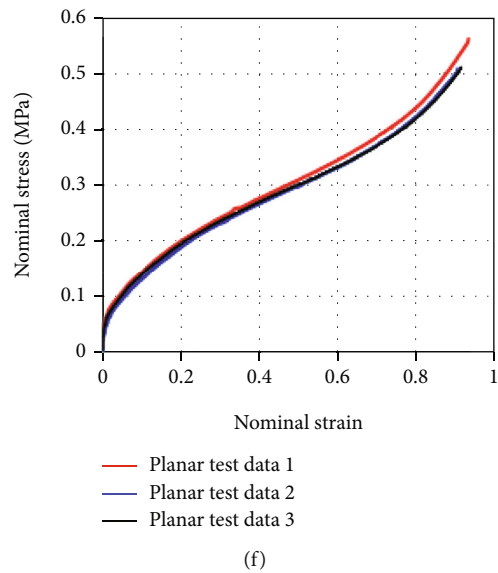
(c)



(d)



(e)



(f)

FIGURE 9: Hyperelasticity test equipment and results. (a) Uniaxial tensile test. (b) Uniaxial tensile curves. (c) Equal biaxial tensile test. (d) Equal biaxial tensile curves. (e) Plane tensile test. (f) Plane tensile curves.

TABLE 3: Mooney-Rivlin model constitutive parameters.

Material model coefficient	C_{10}	C_{01}	$1/D_1$
Value	0.1197	0.0160	0.0



FIGURE 10: Dynamic mechanical analyzer.

play a decisive role in the reliability of finite element analysis results. Rubber material has both hyperelasticity and viscoelasticity. Since rubber has nonlinear properties, it is important to test the rubber before FEA to obtain accurate stress-strain relationships and dynamic response characteristics.

4.1. Hyperelasticity Test. The primary purpose of the hyperelasticity test is to determine the stress-strain relationship of the rubber. To ensure the accuracy of finite element analysis, it is required to collect test data under various strain states.

The uniaxial tensile test, biaxial tensile test, and plane tensile test were carried out using Tsinghua University's testing equipment. The rubber used in the test is silicone rubber from the Institute of Aerospace Materials and Processes' Z-37 series. The thickness of the rubber samples used for the three kind of tensile tests is depicted as 2 mm in the picture. The reflective strip is used to measure the strain of the rubber sample, and it is adhered to the location of the solid red line in Figure 8. Each type of tensile test was conducted in three groups, with the mean value being the test result.

Figure 9 presents uniaxial tensile testing equipment, equal biaxial tensile testing equipment, and plane tensile testing equipment. The objective of the uniaxial tensile test is to determine the stress-strain curve of specimens of rubber under pure tensile stress. Utilizing sixteen in-plane actuators, the biaxial tensile test may evaluate the compression strain state of rubber material. During the test, it must be assured that all actuators apply the same force on the rubber sample and that the resultant force is 0. The objective of the plane tensile test is to evaluate the state of shear strain in rubber. In the plane tensile test, the dimensions of the specimens in the tensile direction are significantly lower than those in the breadth direction. In order to produce a strain state of simple shear deformation and measure the shear modulus of the rubber specimen, it is necessary to provide a complete constraint in the transverse direction of the specimens such that all shear occurs in the

thickness direction. The specimens of rubber were examined at a strain rate of 1% per second. Six times each of 25%, 50%, 75%, and 100% strain tests were conducted in order to eliminate the Mullins effect.

The stress-strain curve obtained through the above material tests is the engineering stress-strain relationship. The relation between nominal stress and nominal strain should be obtained when defining the material's stress-strain curve. It is assumed that the length before the tensile force F is L_0 and the cross-sectional area before the tensile action is A_0 . In the process of tensile action, it is assumed that the material volume remains unchanged, the length is L , and the cross-sectional area is A . We can get the nominal stress $\sigma_n = F/A_0$, engineering stress $\sigma = F/A$, nominal strain $\varepsilon_n = \Delta l/l_0$, and engineering strain $\varepsilon = \Delta l/l$.

The relationship between engineering stress and strain and nominal stress and strain is as follows:

$$\varepsilon = \frac{\Delta l}{l} = \frac{\int_{l_0}^l dl}{l} = \ln \frac{l}{l_0} = \ln \left(\frac{l_0 + \Delta l}{l_0} \right) = \ln (1 + \varepsilon_n), \quad (7)$$

$$\sigma = \frac{F}{A} = \frac{F A_0}{A_0 A} = \frac{F l}{A_0 l_0} = \frac{F l_0 + \Delta l}{A_0 l_0} = \sigma_n (1 + \varepsilon_n). \quad (8)$$

According to equations (7) and (8), the curves of nominal stress and nominal strain of rubber in the uniaxial tensile test, equal biaxial tensile test, and plane tensile test are derived, as shown in Figure 9.

Assuming that rubber is incompressible and isotropic, the above test data is fitted using the least-squares approach to the Mooney-Rivlin constitutive model. The expression for the constitutive model is as follows:

$$U = C_{10}(\bar{I}_1 - 3) + C_{01}(\bar{I}_2 - 3) + \frac{1}{D_1}(J_{el} - 1)^2. \quad (9)$$

The results of the constant parameters in the strain energy function of the constitutive model obtained by fitting are shown in Table 3.

4.2. Viscoelasticity Test. Dynamic mechanical testing was employed in a DMA tester to investigate the frequency-dependent strain rate dependency of rubber materials. The maker of the analyzer is TA, and its model number is Q800, as indicated in Figure 10. The frequency sweep experiment was performed on ZN-37 silicon rubber at a steady temperature. The experimental temperature was maintained at 25°C or room temperature. The sweep frequency range was 1–200 Hz. The step length of the frequency sweep was 1 Hz, and the amplitude was 20. Figure 11 depicts the frequency-dependent energy storage modulus, loss modulus, and damping factor of rubber material.

The results of the tests indicate that the energy storage modulus, loss modulus, and damping factor all vary with frequency, and the nonlinear properties are robust. For numerical simulation, the correlations between storage modulus, loss modulus, and frequency were directly incorporated into the Abaqus material model.

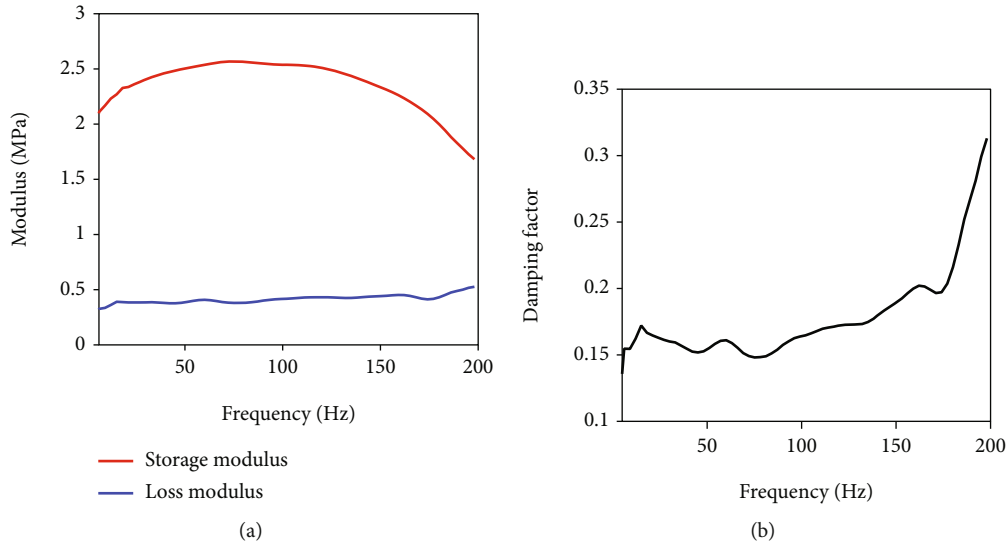


FIGURE 11: Material dynamic viscoelastic test results. (a) Energy storage modulus and loss modulus. (b) Damping factor.

5. Indoor Vibration Test and Finite Element Analysis

5.1. Indoor Vibration Test. As seen in Figure 12, the vibration test of the block of equivalent mass was conducted on the shaking table to validate the vibration-damping effect of the T-rubber isolator. The T-rubber isolator was bolted to the disc fixture, and the mass block was bolted to the table of the shaking table via the disc fixture. Figure 13 shows the layout of measuring points on the vibration table and the state of the rubber shock absorber's installation. Vibration tests were conducted in the horizontal (X and Y) and vertical (Z) directions, respectively, by altering the shaking table's vibration direction. The frequency sweep range was 5–200 Hz, and the experimental vibration magnitudes were 0.2 g, 0.5 g, and 1 g, respectively.

5.2. Finite Element Simulation Analysis

5.2.1. Selection of Rubber Material Model. In the absence of appropriate testing equipment to evaluate the material's nonlinear properties, the rubber analysis must be simplified, i.e., using the parameters in the material performance specification. The rubber material utilized in this test is the ZN-37 series of silicone rubber developed by the Institute of Aerospace Materials and Technology. Table 4 displays the parameters of the silicone rubber's material performance specification.

The rubber's material parameters in Abaqus require elastic Young's modulus E and shear modulus G , and the relationship between them can be expressed as follows:

$$E = 2G(1 + \mu). \quad (10)$$

For incompressible materials, Poisson ratio μ is 0.5.

According to the viscoelastic test results, the damping property of rubber also exhibits nonlinearity. When the loss factor of rubber is known, it can be expressed by the relationship between the material loss factor and Rayleigh damping.

$$C = \alpha M + \beta K. \quad (11)$$

The parameters α and β are related to the free vibration frequencies ω_1 , ω_2 , and damping ratio ξ , which can be written as follows:

$$\begin{Bmatrix} \alpha \\ \beta \end{Bmatrix} = \frac{2\xi}{\omega_1 + \omega_2} \begin{Bmatrix} \omega_1 \omega_2 \\ 1 \end{Bmatrix}. \quad (12)$$

The damping ratio ξ at the resonance peak position is half of the material loss factor. The free vibration frequencies ω_1 and ω_2 should be selected within the required range. The parameters in Rayleigh damping are obtained: $\alpha = 0.78431$, $\beta = 0.00025$.

The description of material model 1 follows. In the numerical analysis, rubber is described using the linear elastic material model. In Abaqus, the mode superposition approach is utilized to solve steady-state dynamics and modal response in the frequency domain.

The description of material model 2 follows. To improve the precision of rubber analysis, its nonlinear stress-strain characteristics must be considered. The nonlinear stress-strain characteristic of rubber is defined using the hyperelastic model determined by the tensile experiments mentioned in Section 4. The loss factor is used to characterize the material's damping property.

The description of material model 3 follows. The tensile test measures the hyperelastic model, which represents the rubber's nonlinear response to stress and strain. Under dynamic load, the dynamic analyzer analyzes viscoelasticity, which characterizes the nonlinear behavior of the complex modulus of the rubber.

5.2.2. Finite Element Model. To ensure the dependability of the analysis and test, a basic equivalent mass block model is created at the early design phase, adopting the same mass and installation size as the radar system. In

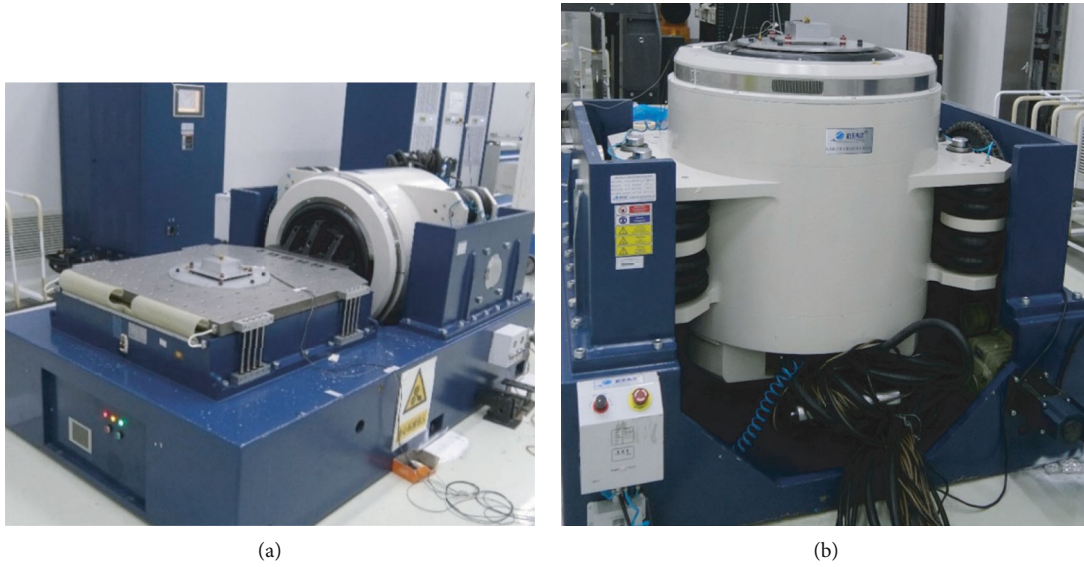


FIGURE 12: Vibration test in all directions. (a) Vibrate horizontally in the X and Y directions. (b) Vertical vibration in the Z direction.

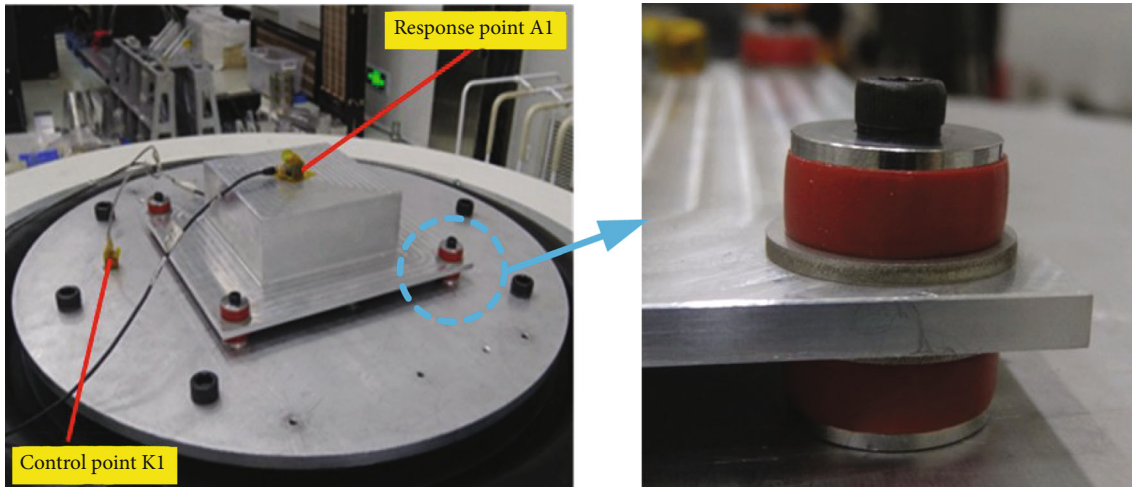


FIGURE 13: Test preparation position and installation status.

TABLE 4: Silicone rubber material parameters.

Material no.	Density (t/mm ³)	Elastic shear modulus (MPa)	Loss factor
ZN-37	1E-9	1	0.2

addition, the T-rubber isolator’s characteristics can be evaluated and tested using the finite element model. The model of the rubber isolation platform is depicted in Figure 14.

The material parameters of each component of the isolator used in the test are shown in Table 5. Input the following material parameters into the finite element software for analysis calculation. Vibration response curves for the three analysis methods are obtained using finite element analysis. The dynamic implicit analysis is implemented in Abaqus with a time step of 0.0001 and an analysis duration of 5 s. The frequency range of the sine sweep is 0–200 Hz, with an amplitude of 0.2 g, 0.5 g, and 1.0 g, respectively.

In addition, mesh convergence is explored under the frequency sweep condition. Using elements ranging in size from 0.8 mm to 1.5 mm, the location of the rubber isolator is discretized. Figure 15 demonstrates that there is no statistically significant difference in the peak response of elements of different sizes. In terms of peak frequency, Figure 15 illustrates that convergence can be attained with an element size of 1 mm. It will take longer to calculate the results if you reduce the size of the pieces further. There will be little change in the outcomes.

5.3. Results and Discussion. Figure 16 shows a comparison between the numerical and experimental results of three material models in three orientations. Comparing the results of the three material models in the Z direction to those in the X and Y directions, it is evident that significant differences exist. The numerical model with material model 3 is able to more accurately characterize the rubber material and produce findings that are more comparable to the

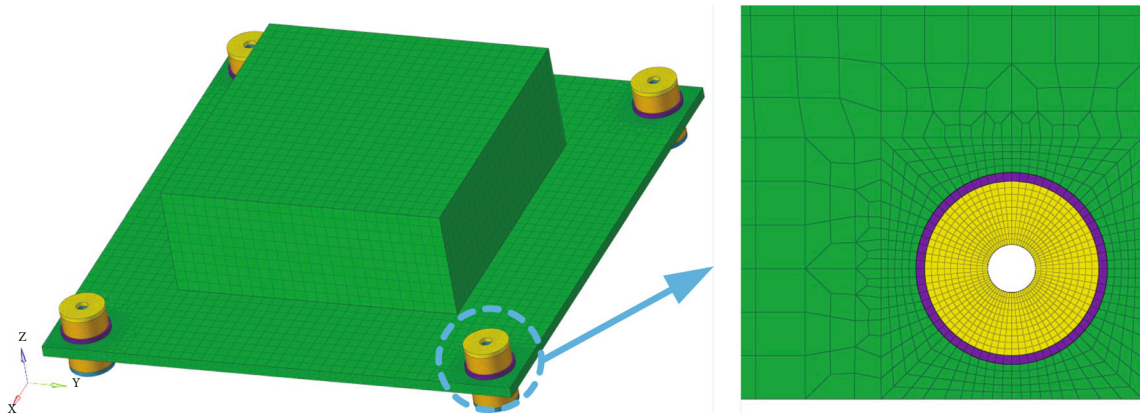


FIGURE 14: Finite element model with 0.8 mm element size.

TABLE 5: Material parameters of each component of the mass block.

No.	Component	Material	Density (t/mm^3)	Elastic shear modulus (MPa)
1	Mass block	AL7050	$2.8E-9$	$7.2E4$
2	Gasket	Q235	$7.8E-9$	$2.1E5$
3	Sleeve	Q235	$7.8E-9$	$2.1E5$
4	Retaining ring	Q235	$7.8E-9$	$2.1E5$
5	Rubber	ZN-37	$1E-9$	/

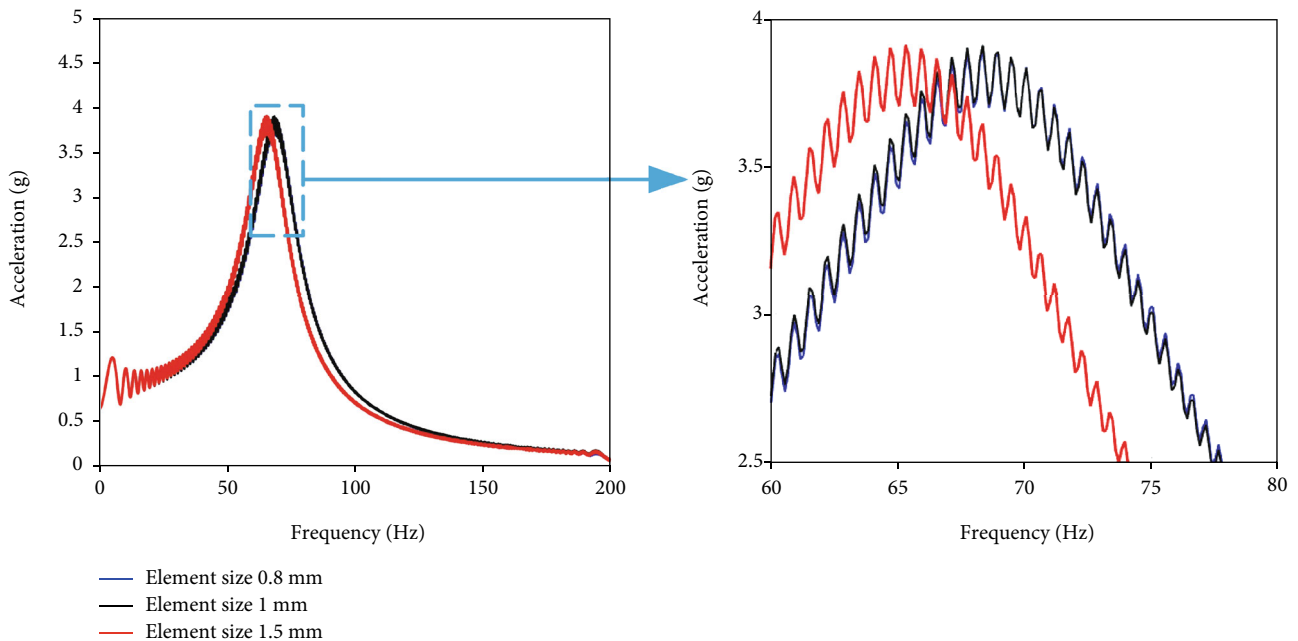


FIGURE 15: Results of different element sizes under sweep frequency condition with 1.0 g amplitude.

experiment. Consequently, the results in the Z direction were employed for subsequent data comparisons.

The experimental and simulation results reveal the vibrational features of the mass block model. The resonance phenomenon is formed close to the first peak frequency, and the vibration response has an amplifying impact. After the

peak frequency, the intensity of the vibration decreases, indicating that the shock absorber is functioning.

The material of model 1 rubber is characterized by linear elasticity and material loss factor. The analysis approach reveals that the peak frequency of the first order hardly varies with vibrations of 0.2 g, 0.5 g, and 1 g. At 100 Hz

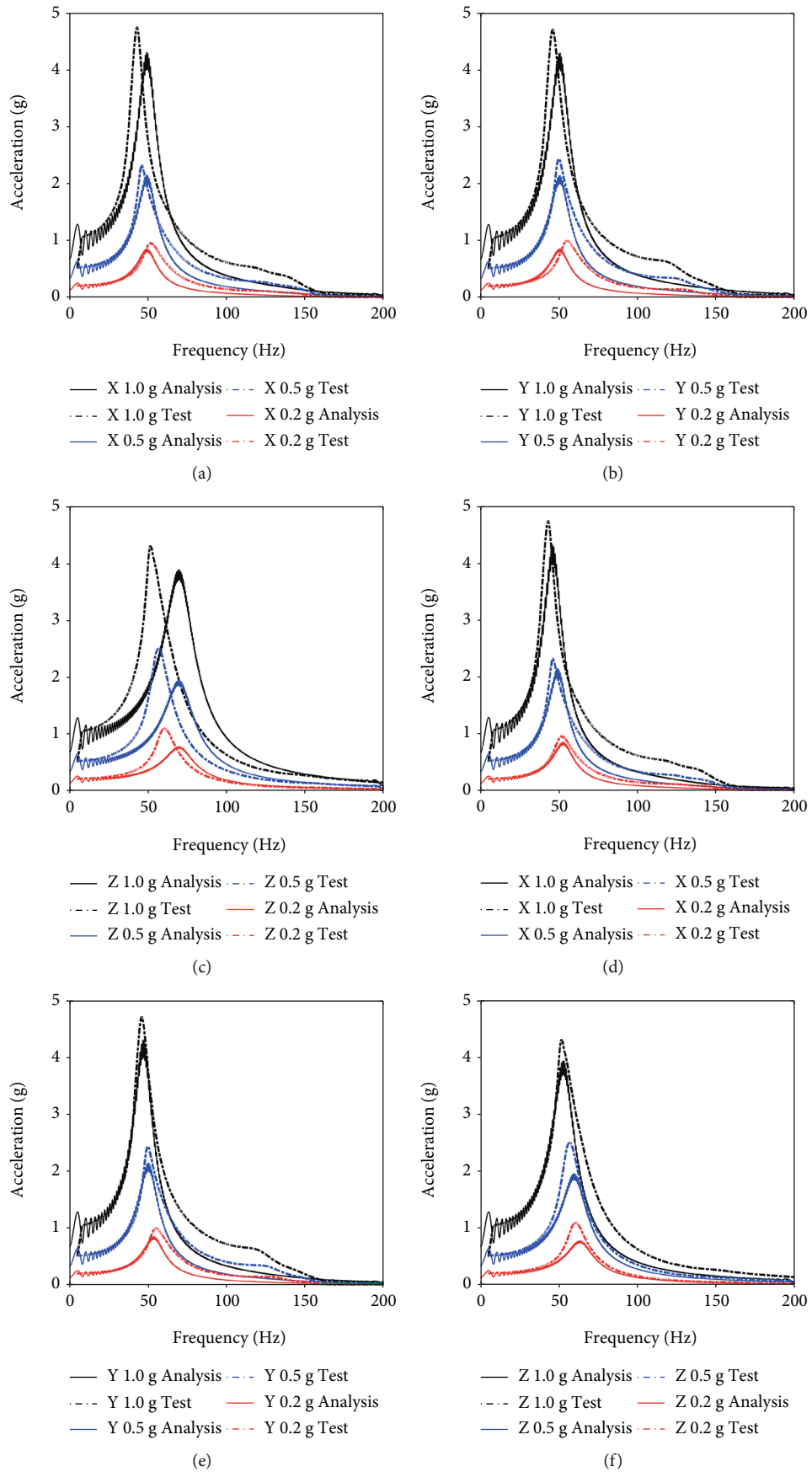


FIGURE 16: Continued.

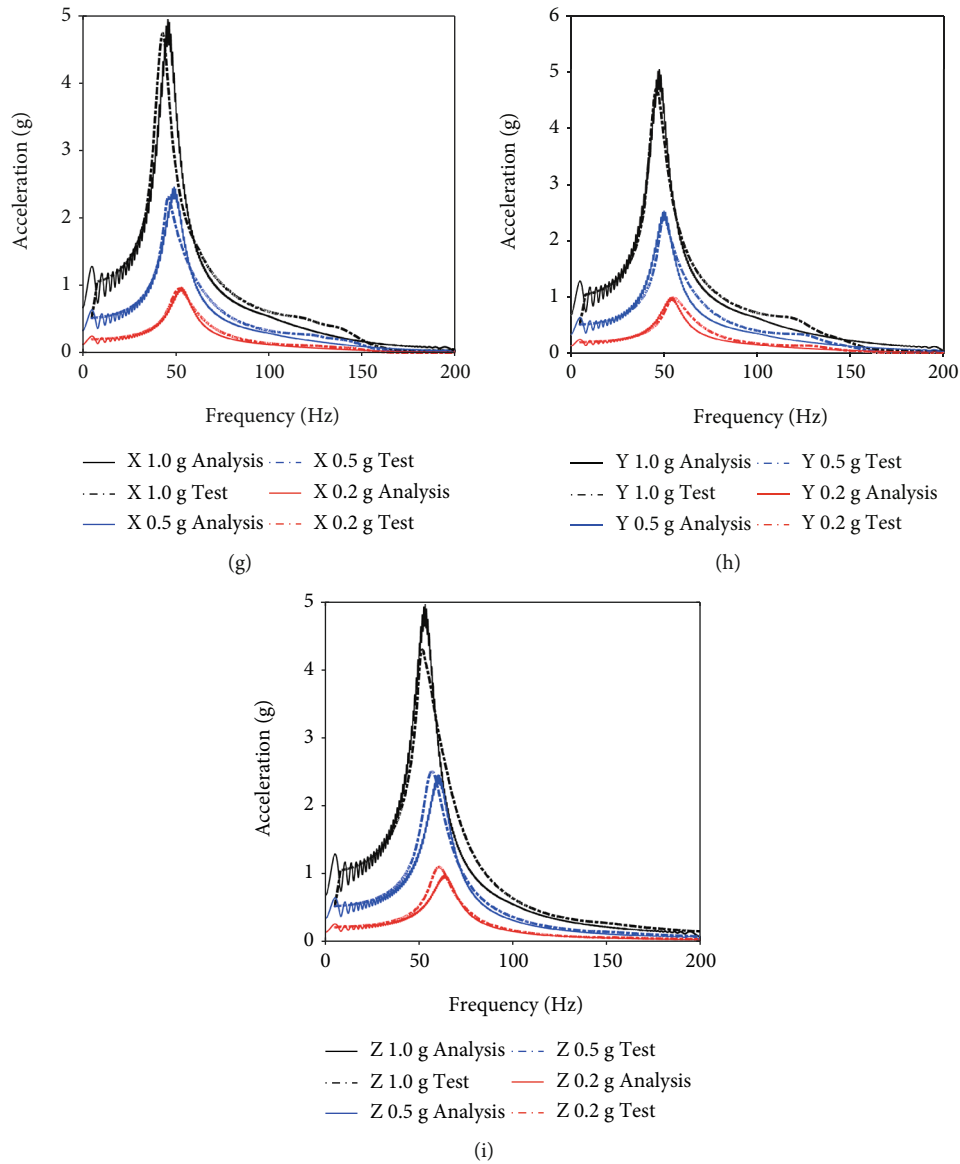


FIGURE 16: Comparison curves of simulation test with different magnitudes. (a) Material model 1 and X direction. (b) Material model 1 and Y direction. (c) Material model 1 and Z direction. (d) Material model 2 and X direction. (e) Material model 2 and Y direction. (f) Material model 2 and Z direction. (g) Material model 3 and X direction. (h) Material model 3 and Y direction. (i) Material model 3 and Z direction.

TABLE 6: Z direction simulation and test comparison of model 1.

	First order peak frequency (Hz)			Peak magnification			100 Hz amplitude reduction effect		
	0.2 g	0.5 g	1.0 g	0.2 g	0.5 g	1.0 g	0.2 g	0.5 g	1.0 g
Simulation	70.07	70.06	70.00	3.89	3.87	3.92	7.92	7.96	7.90
Test	60.03	56.96	51.57	5.49	5.01	4.30	19.59	28.32	36.97
Error (%)	16.72	23.00	35.74	29.14	22.75	8.84	59.57	71.89	78.63

TABLE 7: Z direction simulation and test comparison of model 2.

	First order peak frequency (Hz)			Peak magnification			100 Hz amplitude reduction effect		
	0.2 g	0.5 g	1.0 g	0.2 g	0.5 g	1.0 g	0.2 g	0.5 g	1.0 g
Simulation	63.48	59.57	53.22	3.91	3.93	3.94	32.74	43.83	60.11
Test	60.03	56.96	51.57	5.49	5.01	4.30	19.59	28.32	36.97
Error (%)	5.75	4.58	3.20	28.78	21.56	8.37	67.13	54.77	62.59

TABLE 8: Z direction simulation and test comparison of model 3.

	First order peak frequency (Hz)			Peak magnification			100 Hz amplitude reduction effect		
	0.2 g	0.5 g	1.0 g	0.2 g	0.5 g	1.0 g	0.2 g	0.5 g	1.0 g
Simulation	63.23	60.30	53.53	4.89	4.90	4.97	27.39	38.57	46.15
Test	60.03	56.96	51.57	5.49	5.01	4.30	19.59	28.32	36.97
Error (%)	5.33	5.86	3.80	10.93	2.20	15.58	39.82	36.19	24.83

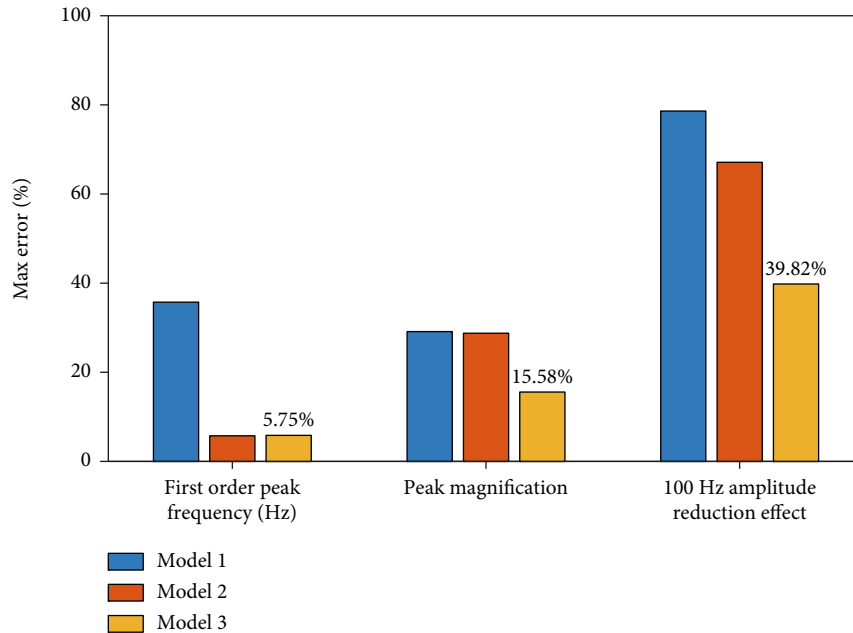


FIGURE 17: The maximum error under the corresponding evaluation index of three material models.

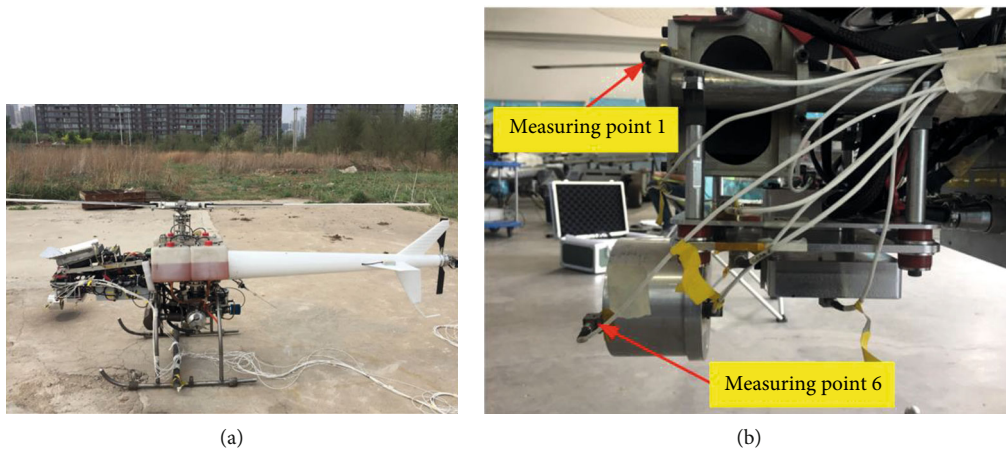
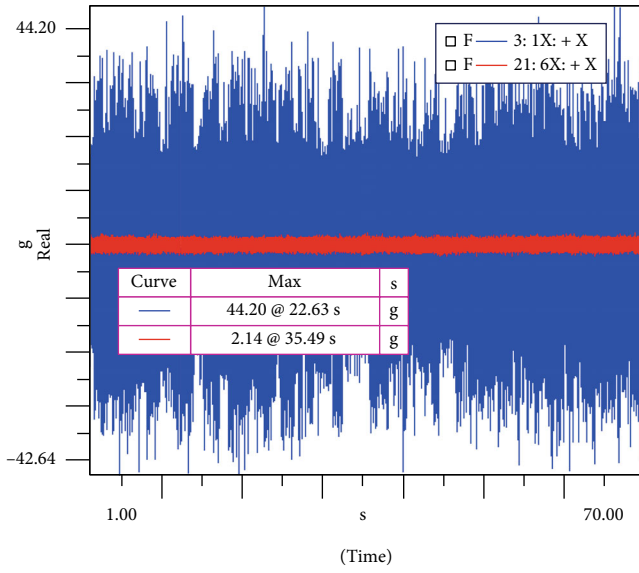


FIGURE 18: Outfield flight test. (a) UAV prototype. (b) Installation of platform and the location of the measuring points.

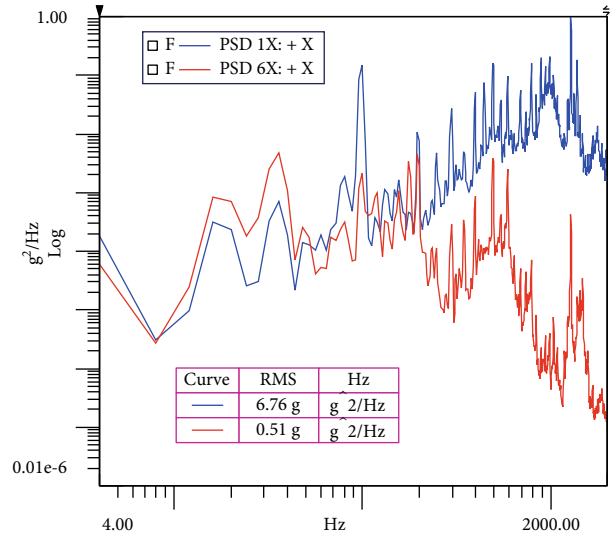
and maximal magnification, the effect of vibration reduction remains approximately linear. However, experimental observations indicate that the first-order peak frequency drops with increasing amplitude and frequency drift occurs at various magnitudes. The peak magnification likewise falls as the magnitude increases. The 100 Hz drop in vibration amplitude increases as the magnitude of the vibration increases.

For model 2, the peak frequency drift phenomenon may be accurately quantified using the hyperelastic model and material-damping factor in the calculation for vibration magnitudes of 0.2 g, 0.5 g, and 1 g.

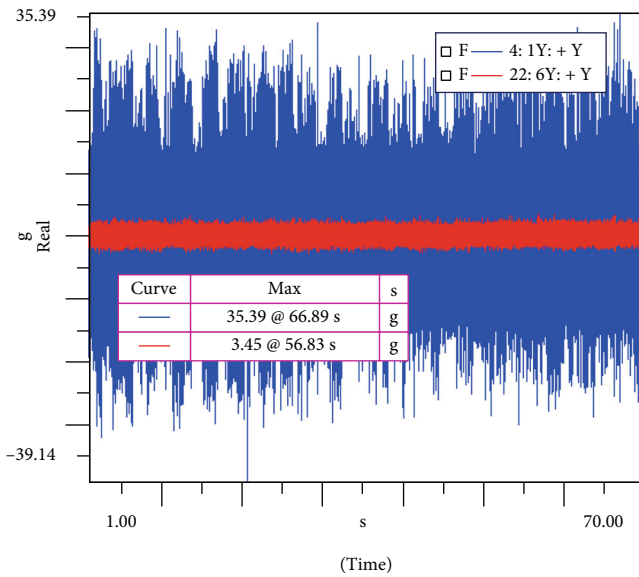
For model 3, using the hyper-viscoelastic model to calculate, the frequency drift phenomena of the peak frequency can be well defined in the calculation under vibration magnitudes of 0.2 g, 0.5 g, and 1 g, demonstrating the material's



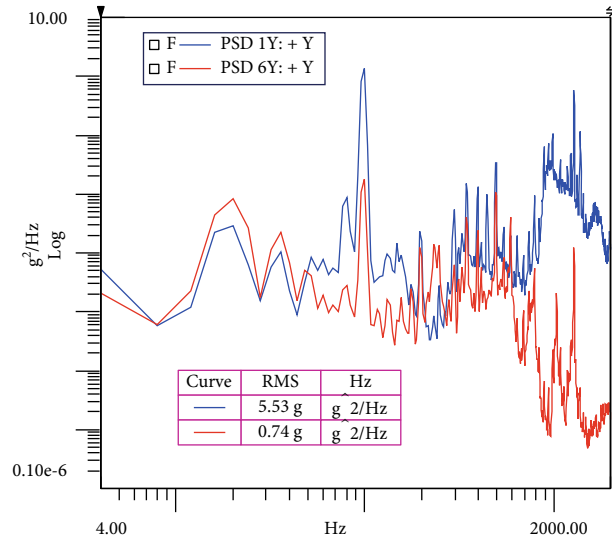
(a)



(b)



(c)



(d)

FIGURE 19: Continued.

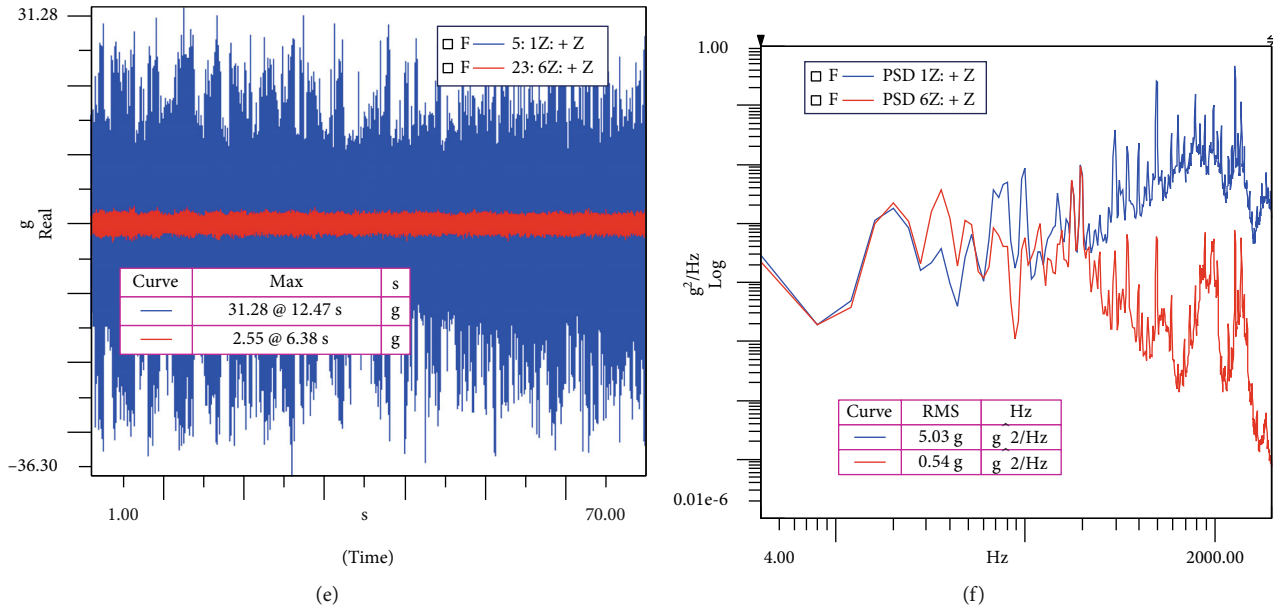


FIGURE 19: Field test result. (a) X direction time-domain response. (b) X direction frequency-domain response. (c) Y direction time-domain response. (d) Y direction frequency-domain response. (e) Z direction time-domain response. (f) Z direction frequency-domain response.

nonlinear nature. The vibration reduction impact at 100 Hz increases with increasing magnitude, which is likewise well defined and most compatible with actual test results. Clearly, model 3's data error is smaller than model 2's, as evidenced by the graph.

The first-order frequency peak, peak amplification factor, and vibration reduction effect at 100 Hz are determined by examining the vibration response curves of the three material models in the Z direction generated by finite element analysis. Tables 6–8 depict, accordingly, the comparison of simulation and test results for the three models.

From the aforementioned three tables, we can get Figure 17, which depicts the greatest discrepancy between the outcomes of an experiment and a computer simulation, using the same evaluation index for each model.

Intuitively, Figure 17 suggests that material model 3, i.e., the hyper-viscoelastic material model, is better appropriate for the characterization of rubber. The numerical simulation with material model 3 demonstrates good performance across all three assessment indices, which is the most congruent with the experimental findings. In terms of first-order peak frequency, the maximum inaccuracy of material model 1 is 35.74 percent, whereas those of material models 2 and 3 are 5.75 percent and 5.86 percent, respectively. In terms of maximum magnification, material model 2 is 28% whereas model 3 is only 15.58%. Finally, the 100 Hz inaccuracy in the amplitude reduction was detected. The greatest error of material models 1 and 2 was 78% and 67%, respectively, whereas material model 3 had a maximum error of only 39.82%. The frequency response curve also reveals that the three simulation findings of the material model are comparable to the experimental data. Using material model 3, a more precise finite element model can be created. Specifically, the hyperelastic model describes the nonlinear features of stress and strain of rubber material, whereas the viscoelas-

tic model describes the nonlinear properties of the complex modulus of rubber under dynamic load. In addition, testing and finite element analysis demonstrate that the rubber isolator can dampen the vibration transmitted from the fuselage to the radar at 100 Hz and its multiple frequencies.

6. Vibration Performance Test of Airborne Radar with Rubber Isolator

6.1. Flight Test Preparation. As seen in Figure 18(a), the T-type rubber isolator is mounted on an actual UAV prototype for flight testing. The radar and T-type rubber isolators are mounted on the UAV's front. During flight, the acceleration sensor receives radar and fuselage vibration signals. Figure 18(b) illustrates the arrangement of measurement point 1 on the UAV fuselage and measuring point 6 on the radar.

In Figure 18(b), measuring point 6 corresponds to the radar installation location, where the vibration absorber is operational, and measuring point 1 corresponds to the UAV fuselage, where the vibration is generated.

6.2. Flight Test Result. The outside flight test of the UAV is equivalent to the actual working environment. Figure 19 displays the time-domain response and frequency-domain response of the three directions acquired after flight stabilization.

From the vibration response in the frequency domain of different directions, it can be shown that the vibration isolation platform at low frequency exhibits a resonance phenomenon that generates an amplification effect. After 100 Hz, however, the effect of reducing vibrations becomes increasingly apparent, and the vibration response at point 6 is clearly decreasing compared to the response at point 1, indicating that the vibration absorber is functioning properly.

TABLE 9: Data comparison of vibration reduction performance.

Direction	Measuring point A1		Measuring point A6		Vibration reduction efficiency
	Time-domain response (g)	RMS acceleration (g)	Time-domain response (g)	RMS acceleration (g)	
X	43.75	6.84	3.24	0.51	92.55%
Y	33.88	4.88	5.45	0.95	80.54%
Z	29.45	4.96	3.31	0.60	87.91%

Table 9 displays the vibration response results obtained during the airborne phase of the UAV's actual flight test. At measuring point 1, where the vibration is generated, the values for the greatest acceleration response in the time domain are 44.20 g in the X direction, 35.39 g in the Y direction, and 31.28 g in the Z direction. The root-mean-square acceleration values in the X direction are 6.76 g, in the Y direction, they are 5.53 g, and in the Z direction, they are 5.03 g. The aforementioned vibration responses all exceed the radar environment's criteria. At measuring point 6, which is affected by the vibration isolator, the vibration response results are as follows: the maximum acceleration response results in the time domain are 2.14 g in the X direction, 3.45 g in the Y direction, and 2.55 g in the Z direction, and the root-mean-square acceleration values are 0.51 in the X direction, 0.74 g in the Y direction, and 0.54 g in the Z direction. 92.46 percent, 86.62 percent, and 89.24 percent, respectively, are the vibration reduction efficiencies of the three directions. Following the application of the vibration absorber, a significant reduction in vibration is realized.

7. Conclusions

In this paper, the vibration acceleration signal of a UAV during flight was collected, from which it was determined that the frequency of the UAV flight vibration signal is predominantly distributed at 100 Hz and its multiple frequencies. Under the frequency sweep condition of 200 Hz, numerical simulation and indoor experiment on the corresponding UAV vibration isolation platform are conducted. Then, it was determined that the proposed T-type rubber isolator reduces the vibration generated by the UAV to the radar effectively. In addition, we obtain a more accurate model of the rubber material by comparing the FEM findings with the experimental data. The nonlinear characteristics of stress and strain of rubber are characterized by the Mooney-Rivlin hyperelastic model, and the nonlinear characteristics of the complex modulus of rubber under dynamic load are characterized by the generalized Maxwell viscoelastic model when constructing an accurate finite element model. Finally, a real outdoor flight test was carried out. After the vibration absorber is applied, the vibration reduction phenomenon can be clearly seen through the frequency-domain PSD curves. Due to the complexity of the vibration environment, the vibration response amplitude at the first peak of the PSD curve increases with increasing vibration frequency, resulting in an amplifying effect at low-order frequency. The vibration absorber is effective at isolating vibrations at high frequencies. The frequency-domain PSD curves reveal that,

despite the higher power spectral density peaks in the high-frequency region, the vibration response in the frequency range has a greater attenuation than the peak PSD without the T-type rubber isolator. During the flight test, it is evident from the time-domain curves that the vibration absorber operates effectively in the whole time domain.

Data Availability

The data from this manuscript may be made available upon request to the authors.

Disclosure

An earlier research outcome of this project has been presented by Yu Changshuai et al. as a Conference Paper in the Vibration Test and Vibration Reduction Design of UAV Load Radar. We hereby declare this paper and the previous conference paper belong to the same project and inherit its follow-up work. However, this paper pays more attention to the selection of appropriate rubber material constitutive model to improve the accuracy of numerical simulation.

Conflicts of Interest

The authors declare that there are no conflicts of interest regarding the publication of this paper.

Acknowledgments

This article is funded by the following fund projects: the National Natural Science Foundation of China (NSFC) (51975567); the Liaoning Revitalization Talents Program (XLYC1907152); the Natural Science Foundation of Liaoning Province (2019-MS-347); the Autonomous Fund Project of the State Key Laboratory of Robotics (2022-Z01); the Youth Innovation Promotion Association of the Chinese Academy of Sciences [2018237]; and the Jiang Xin-song Innovation Fund [20180504]. I would like to thank Yu Changshuai et al. for doing some research at the beginning of this project.

References

- [1] Y. He and Y. C. Zhang, "Current situation and development trend of agricultural UAV," *Modern Agricultural machinery*, vol. 1, pp. 1–5, 2014, (In Chinese).
- [2] L. Liu and B. Ji, "Current situation and development trend of UAV-based radar," *Modern Navigation*, vol. 3, pp. 227–230, 2014, (In Chinese).

- [3] M. Du, "Future - oriented U. S. unmanned reconnaissance system," *Modern Weaponry*, vol. 9, pp. 27–29, 1998, (In Chinese).
- [4] J. Langelaan and S. Rock, "Navigation of small UAVs operating in forests," in *AIAA Guidance, Navigation, and Control Conference and Exhibit*, p. 5140, Providence, Rhode Island, 2004, (In Chinese).
- [5] B. Sinopoli, M. Micheli, G. Donato, and T. J. Koo, "Vision based navigation for an unmanned aerial vehicle," in *In Proceedings 2001 ICRA. IEEE International Conference on Robotics and Automation*, vol. 2, pp. 1757–1764, Seoul, Korea (South), 2001.
- [6] S. K. Phang, F. Wang, K. Wang, S. Lai, and B. M. Chen, "An effective method for autonomous localization and navigation in unknown indoor environment using mav," in *International Micro Air Vehicles Conference*, Aachen, Germany, 2015.
- [7] N. Patrizi, G. Fragkos, K. Ortiz, M. Oishi, and E. E. Tsiropoulou, "A UAV-enabled dynamic multi-target tracking and sensing framework," in *GLOBECOM 2020-2020 IEEE Global Communications Conference*, pp. 1–6, Taipei, Taiwan, 2016.
- [8] Z. Li, M. Lao, S. K. Phang, M. R. Hamid, K. Z. Tang, and F. Lin, "Development and design methodology of an anti-vibration system on micro-UAVs," in *International micro air vehicle conference and flight competition(IMAV)*, pp. 223–228, Toulouse, France, 2017.
- [9] M. Baskin and M. K. Leblebicioğlu, "Robust control for line-of-sight stabilization of a two-axis gimbal system," *Turkish Journal of Electrical Engineering & Computer Sciences*, vol. 25, pp. 3839–3853, 2017.
- [10] J. Windau and L. Itti, "Multilayer real-time video image stabilization," in *2011 IEEE/RSJ International Conference on Intelligent Robots and Systems*, pp. 2397–2402, San Francisco, CA, USA, 2011.
- [11] F. La Rosa, M. C. Virzi, F. Bonaccorso, and M. Branciforte, "Optical image stabilization (OIS)," STMicroelectronics. Available online: http://www.st.com/resource/en/white_paper/ois_white_paper.pdf, 2015.
- [12] M. G. Song, Y. J. Hur, N. C. Park et al., "Design of a voice-coil actuator for optical image stabilization based on genetic algorithm," *IEEE Transactions on Magnetics*, vol. 45, no. 10, pp. 4558–4561, 2009.
- [13] Z. Xu, S. Pan, L. Chen, and Z. Xiao, "A double gimbal optical image stabilizer driven by piezoelectric stacks," *Review of Scientific Instruments*, vol. 92, no. 4, article 045008, 2021.
- [14] S. Erturk, "Digital image stabilization with sub-image phase correlation based global motion estimation," *IEEE Transactions on Consumer Electronics*, vol. 49, no. 4, pp. 1320–1325, 2003.
- [15] M. Kim, G.-S. Byun, and G.-H. Kim, "Gimbal system control for drone for 3D image," *Journal of the Korea Institute of Information and Communication Engineering*, vol. 20, no. 11, pp. 2107–2112, 2016.
- [16] C. Dahlin Rodin, F. A. de Alcantara Andrade, A. R. Hovenburg, and T. A. Johansen, "A survey of practical design considerations of optical imaging stabilization systems for small unmanned aerial systems," *Sensors*, vol. 19, no. 21, p. 4800, 2019.
- [17] M. Verma, V. Lafarga, M. Baron, and C. Collette, "Active stabilization of unmanned aerial vehicle imaging platform," *Journal of Vibration and Control*, vol. 26, no. 19–20, pp. 1791–1803, 2020.
- [18] C. Liu, X. Jing, S. Daley, and F. Li, "Recent advances in micro-vibration isolation," *Mechanical Systems and Signal Processing*, vol. 56–57, no. 56, pp. 55–80, 2015.
- [19] A. E. Pete, D. Kress, M. A. Dimitrov, and D. Lentink, "The role of passive avian head stabilization in flapping flight," *Journal of the Royal Society Interface*, vol. 12, no. 110, article 20150508, 2015.
- [20] J. Guo, X. R. Zeng, and Q. K. Luo, "Research progress of rubber damping materials," *Special Purpose Rubber Products*, vol. 28, no. 7, pp. 175–178, 2012.
- [21] Y. Huang, S. H. Yang, X. U. Lei, G. E. Xinling, S. U. Zhengtao, and W. A. Jinghe, "Research and application progress of silicone rubber materials in aviation," *Journal of aeronautical materials*, vol. 36, no. 3, pp. 79–91, 2016.
- [22] M. Zhongbiao, Z. Zhenzhen, and G. Cheng, "Research progress of silicone rubber damping materials," *World rubber industry*, vol. 40, no. 1, pp. 15–19, 2016.
- [23] S. Chen, M. Xuan, J. Xin et al., "Design and experiment of dual micro-vibration isolation system for optical satellite flywheel," *International Journal of Mechanical Sciences*, vol. 179, article 105592, 2020.
- [24] Z. D. Xu, Y. X. Liao, T. Ge, and C. Xu, "Experimental and theoretical study of viscoelastic dampers with different matrix rubbers," *Journal of Engineering Mechanics*, vol. 142, no. 8, 2016.
- [25] E. M. Arruda and M. C. Boyce, "A three-dimensional constitutive model for the large stretch behavior of rubber elastic materials," *Journal of the Mechanics and Physics of Solids*, vol. 41, no. 2, pp. 389–412, 1993.
- [26] R. S. Rivlin, "Large elastic deformations of isotropic materials IV. Further developments of the general theory," *Philosophical transactions of the royal society of London. Series A, Mathematical and physical sciences*, vol. 241, no. 835, pp. 379–397, 1948.
- [27] M. Mooney, "A theory of large elastic deformation," *Journal of Applied Physics*, vol. 11, no. 9, pp. 582–592, 1940.
- [28] O. H. Yeoh, "Some forms of the strain energy function for rubber," *Rubber Chemistry and Technology*, vol. 66, no. 5, pp. 754–771, 1993.
- [29] A. N. Gent, "A new constitutive relation for rubber," *Rubber Chemistry and Technology*, vol. 69, no. 1, pp. 59–61, 1996.
- [30] P. J. Blatz and W. L. Ko, "Application of finite elastic theory to the deformation of rubbery materials," *Transactions of the Society of Rheology*, vol. 6, no. 1, pp. 223–252, 1962.
- [31] R. W. Ogden, "Large deformation isotropic elasticity—on the correlation of theory and experiment for incompressible rubberlike solids," *Proceedings of the Royal Society of London. A. Mathematical and Physical Sciences*, vol. 326, no. 1567, pp. 565–584, 1972.
- [32] Q. S. Xiao, Y. L. Zhao, and Z. Jin, "An equivalent test method for elastomeric constitutive model of rubber material," *Ship Ocean Engineering*, vol. 47, no. 4, pp. 120–124, 2018, (In Chinese).
- [33] B. H. Han, "Measurement and application of rubber material constants based on Mooney-Rivlin model," *China Rubber Industry*, vol. 65, no. 5, pp. 21–25, 2018, (In Chinese).
- [34] J. Q. Li, "A practical numerical algorithm for dynamic response of viscoelastic composite structures," *China Rubber Industry*, vol. 28, no. 2, pp. 25–26, 2001, (In Chinese).
- [35] J. Zhou, Z. G. Yang, and X. L. Feng, "Dynamic viscoelastic analysis and experiment of an aerospace silicone rubber damper based on DMA test," in *2021 the 5th International Conference on Robotics, Control and Automation*, pp. 58–62, Seoul, Republic of Korea, 2021.
- [36] W. F. Zhang, Y. T. Wei, and Y. Li, "Calculation and application of viscoelastic constitutive relation for rubber suspensions," in *Proceedings of the 19th Annual Conference of Beijing Physics Society*, pp. 619–620, Beijing, China, 2013, In Chinese.